AIAA JOURNAL
Vol. 43, No. 9, September 2005

Temporal and Spatial Evolution of a Laser Spark in Air

Nick Glumac,* Gregory Elliott,† and Martin Boguszko‡
University of Illinois at Urbana–Champaign, Urbana, Illinois 61801

Experiments were conducted to quantify the temperature and electron number density of a laser spark formed in air. The laser spark was created by focusing a 180-mJ beam from the second harmonic (wavelength of 532 nm) of a pulsed Nd:YAG laser with a 100-mm focal length lens. For early times, between 50 ns and 1 μs, images of the spark emission have been obtained to characterize the geometry. Also the temperature and electron number density were measured from the emission spectra between 490 and 520 nm where 46 N II lines are observed. The methodology of fitting the experimental data to the modeled spectra to deduce the temperature and electron number density is described. For the initial temporal range, the temperature peaks at approximately 50,000 K and decays over the first 1 μs. The electron number density peaks at approximately 10^{19} cm^{-3}, decaying only slightly slower than t^{-1}. For the longer temporal evolution, from 20 to 1000 μs, planar temperature measurements were achieved using filtered Rayleigh scattering. The peak temperature starts at approximately 4100 K at 20 μs and decays to 580 K by 1 ms. The planar temperature images show a center jet propagating in the opposite direction as the initiating laser beam, which induces a vortex ring (or torus) propagating in the direction of the beam. The evolution of the position and radius of the torus structure is described and fit with a power law utilized by previous investigators. The temperature of the plasma created by laser-induced optical breakdown appears to fit quite well using a triple exponential over the four orders of magnitude of temporal range where measurements were conducted.

Introduction

THERE is a growing interest in the utilization of plasmas in aerodynamics, particularly for high-speed flow applications where the consideration of compressibility is a significant aspect of the problem. Investigation in the utilization of plasmas for aerodynamic research was initiated by the experiments of Klimov et al.,[1] who demonstrated that the strength of a propagating normal shock is reduced in the presence of a weakly ionized flow. Also initial experiments by Gordeev et al.[2] suggested that aerodynamic drag can be significantly reduced by initiating a plasma in front of a body placed in supersonic flow. Even though much research has been conducted suggesting that the mechanism for these effects was mostly thermal instead of electromagnetic, there is still a variety of applications where plasmas can be used for aerodynamic flow control.[3] These aerodynamic applications generally utilize continuous or pulsed plasmas that have been initiated by microwaves or by laser-induced optical breakdown (also termed a laser spark). Applications of the introduction of plasmas for aerodynamic flow control include control of large-scale structures in compressible shear layers,[4,5] creation of virtual cowl inlets,[6] creation of virtual thermal forebodies for sonic boom reduction,[7] and control of shock waves and their interactions.[3,8–12] The majority of the experimental studies conducted utilize laser-induced optical breakdown due primarily to the ease with which the spark timing and location can be controlled. Recent review articles by Knight et al.[13] and Knight[14] give a general overview of the governing equations and applications of plasmas for aerodynamic flow control.

To better understand ongoing applications of laser energy deposition for aerodynamic flow control, there is a need to characterize the laser-induced optical breakdown process, particularly under conditions relevant to these applications. This need is important for the development of computational models to predict the resulting flowfields at both short timescales (with real gas and plasma effects) and long timescales when thermal/fluid dynamic effects dominate the processes.

The formation of laser-induced optical breakdown in a gas has been investigated since its discovery by Maker et al. in 1963 resulting in several studies that have been summarized by Raizer,[15,16] Morgan,[17] and Smith.[18] As described by Raizer,[15,16] the photon-initiated electron cascading plasma process begins when a pulsed laser beam is focused down to a point (or more rigorously, a small region of space), which produces a very sudden temperature rise in the fluid at that point. If the electric field of the laser radiation near the focus becomes greater than that of the binding electrons to their nuclei, it will trigger the breakdown of the air molecules and produce the ionization of the gas. This breakdown causes a cascade effect because the plasma becomes opaque to the laser so that more of the energy is absorbed. As outlined by Adelgren et al.,[9] the energy deposition into a gas by a focused laser beam can be described by four progressive steps: 1) initial release of electrons by multiphoton effect, 2) ionization of the gas in the focal region by the cascade release of electrons, 3) absorption and reflection of laser energy by the gaseous plasma, and 4) formation and propagation of the detonation wave into the surrounding gas and relaxation of focal region plasma. In addition, investigators[9,19] observed a residual vortex ring formed by the asymmetric plasma formation in quiescent air, the cause of which will be described shortly.

Quantitative analysis of the conditions, such as temperature and electron number density, during a laser discharge has also been performed by a number of groups, primarily with respect to applications in the area of laser-induced breakdown spectroscopy (LIBS)[20] for elemental analysis. Many studies have, thus, been made with discharges at, near, or within condensed-phase surfaces. Flow control applications will require discharges at least somewhat removed from the surfaces, and thus, the effect of the surface on the characteristics of the discharge will likely be less than in LIBS. Several papers have addressed such isolated laser discharges in air and various other gases. Radziemski et al.[21] provided a fairly comprehensive early look at laser discharges in the presence of different aerosols. They used emission spectroscopy to measure temperature and electron number density as a function of time for 1064-nm Nd:YAG laser sparks. They report T and N_e density data between 200 ns and 10 μs after the laser spark. There is significant scatter in the temperature data for each of the line pairs used, but the N_e data are fairly consistent. Yalcin et al.[22] follow with a more recent study that examined the effect of ambient conditions (humidity, ambient gas, laser energy) on the temperature and number density in the

Received 1 December 2004; revision received 21 March 2005; accepted for publication 31 March 2005.

*Associate Professor, Mechanical and Industrial Engineering Department.
†Associate Professor, Aerospace Engineering Department.
‡Postdoctoral Research Associate, Aerospace Engineering Department.

spark. They report T and N_e data from 200 ns to 2 μs, although they mention systematic errors with temperature measurements for times less than 1 μs. They discuss the effects of optical depth in their measurements, and they use an Abel inversion technique in some cases to obtain centerline (as opposed to path-averaged) T and N_e.

Chen et al.[23] looked at much earlier times to examine the breakdown phenomenon and the early-time development of the spatial distribution of the plasma. They provide time-resolved images in the period out to 65 ns, but no temperature or electron number density measurements. Nassif and Huwel[24] investigated temperature and spatial structure at much later times in pure nitrogen over a range of pressures and laser energies using Rayleigh scattering showing the development of a well-defined torus at about 100 μs. Additionally, Longenecker et al.[25] investigated temperature and spatial structure at much later times in pure argon, nitrogen, and argon–nitrogen mixtures using Rayleigh scattering and emission spectroscopy. They include imaging and temperature data out to several milliseconds. Both of these studies show images that characterize the radial growth of the spark into a ball, then a disk, followed by the formation of a well-defined torus.

There are at least two significant gaps in the previous work that we attempt to fill with this study. The first is very early temperature and number density data. Previous LIBS studies[26] on titanium surfaces suggest that the electron number density decreases two orders of magnitude in the period 0–200 ns after the laser breakdown and that temperature decreases by a factor of three. Though these studies were at very low pressure, they do highlight the early-time region as a critical period during which rapid changes in the laser-induced plasma occur.

The second area that requires further study is the late-time behavior of the laser spark in air. Though Longenecker et al.[25] do present a limited sequence of images for one condition in argon, there is no detailed information on the long-term, for example, out to tens of milliseconds, progression of the spatial distribution and temperature field of the laser-induced plasma in air.

Experimental Setup and Methodology

Emission Spectroscopy Measurements

To generate the laser spark, a doubled Nd:YAG laser (Spectra Physics Model Quanta Ray GCR 230) provided a beam of 180 mJ per pulse at a wavelength of 532 nm and a repetition rate of 10 Hz. The beam had a greater than 60% Guassian intensity distribution (tending toward a top-hat profile) with a diameter of about 9 mm. The pulse duration was measured to be approximately 6.5-ns full width at half-maximum (FWHM). The laser output frequency was operated in a multimode condition (unseeded) with a frequency line width (FWHM), as given by the manufacturer, of 1.4 cm^{-1} or 42 GHz. The pulse-to-pulse energy stability for this laser is $<3\%$ for $>99\%$ of the pulses over a 1-h period by manufacturer specification with excellent repeatability observed throughout the tests. The laser is focused by a 100-mm focal length planoconvex lens resulting in a net energy of 150 mJ per pulse for each case.

The experimental setup for the optical emission spectroscopy measurements is similar to that of Yalcin et al.[22] and is shown in Fig. 1. Emission from the focal volume is imaged onto the inlet slit of a 270-mm focal length imaging spectrometer (SPEX M270) by a 50-mm-diam, 100-mm-focal-length achromat operating at unit magnification. The entrance slit width was set to 10 μm, and approximately 10 mm of the slit height is imaged vertically onto the detector array. A 1200-grooves/mm grating was used, and the dispersion was 0.068 nm/pixel, resulting in a spectral resolution (2.2 pixels) of 0.15 nm. In the vertical axis, each pixel corresponded to 20 μm in the spark. A gated, intensified charge-couple device (CCD) camera (Roper Scientific PI-MAX) with a 512×512 pixel array served as the detector for the emission spectra measurements and direct imaging of the emission. The emission spark measurements were performed in stationary room air with no filtration or additional preparation. The atmospheric pressure was approximately 740 torr, and the room humidity varied in the 20–40% range over the series of tests.

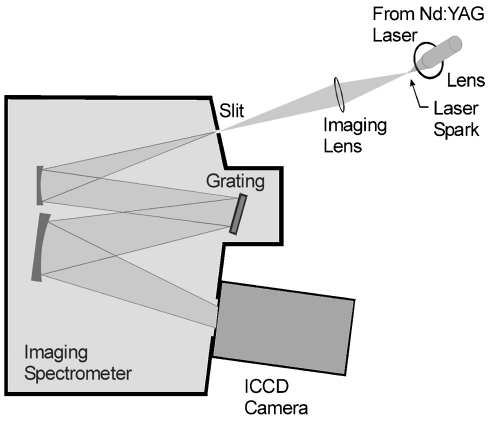

Fig. 1 Schematic of experimental layout for the emission spectroscopy measurements of laser-induced optical breakdown in air.

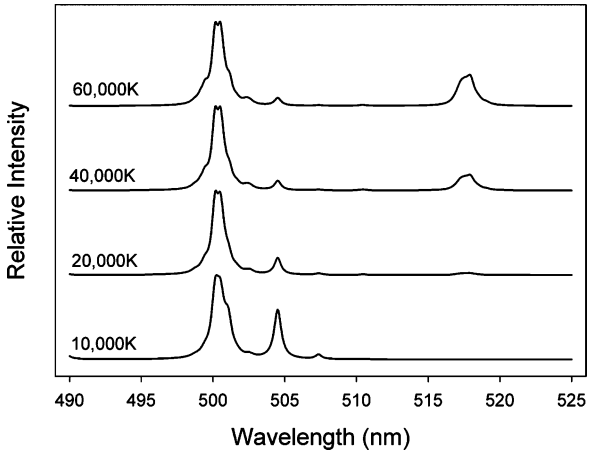

Fig. 2 Modeled emission spectra of N II for measured wavelength range in experiments over expected temperatures for a laser spark in air.

For each time delay, a temporal gate ranging from 41 to 250 ns was applied. The shorter gates were used at earlier times when signal intensity was greatest. Images containing the spatially resolved spectra were ensemble averaged over 200 shots. In our spatially integrated measurements, the images were first binned in the vertical direction and then were processed using calibration frames from a neon lamp and a tungsten intensity calibration lamp.

The spectral region of interest for these measurements is from 490 to 520 nm. In this spectral region over the time period of 0–2 μs from the laser pulse, only N II lines are seen, and the spectrum varies considerably as temperature changes. The 46 lines in this region represent primarily transitions from upper states with energies covering a fairly broad range of wave numbers (169,000–245,000 cm^{-1}). For times shorter than 2 μs, the lines overlap to form three spectral features, as shown in Fig. 2. The main peak near 500 nm consists of a series of transitions mostly from the ^3S, ^5P, and ^3D upper states with energies spanning the middle of the range, from 187,000 to 226,000 cm^{-1}. The second, smaller peak near 504.5 nm is dominated by one line from the $^3P^\circ$ upper state with an energy of 168,892 cm^{-1}, which is the lowest energy level probed. The third feature is a broad peak near 518 nm, which consists of lines from the $^5P^\circ$ and $^5D^\circ$ state with energies around 244,000 cm^{-1}, which is at the high end of the range in this spectrum. Thus, as temperature decreases, the third broad peak becomes smaller, and the second peak becomes more prominent.

The spectra are fitted to a spectral model that yields temperature and electron number density. The model assumes that 1) local thermodynamic equilibrium (LTE) applies for all times considered,

that is, for times longer than 50 ns after the laser pulse, 2) Stark broadening is dominated by electron collisions, and thus, Stark linewidth increases linearly with electron number density, 3) Stark shift also scales linearly with N_e, 4) the observed spectral linewidth can be calculated as a convolution of the instrument, Doppler, and Stark line shapes, 5) the underlying continuum emission below the line spectrum can be approximated by a linear intensity vs wavelength function, and 6) the plasma is uniform in properties along the line of sight probed by the spectrometer. These assumptions follow closely the approach of Hermann et al.,[26] who studied LIBS Ti plasmas in a rarefied environment. Stark widths and shifts for the 46 lines in our spectral are estimated primarily using the data compiled in Ref. 27. Two important exceptions should be noted. The Stark width for the N II line at 504.51 nm appeared to be slightly overestimated in all our spectra where that line was cleanly resolved. The compilation in Ref. 27 quotes a value from Mar et al.,[28] who measured a linewidth of 38 pm at $N_e = 10^{17}$ cm^{-3} and a general uncertainty of 15% on their width measurements. The 38 pm of Mar et al. is significantly higher than the 34 pm of Purcell and Barnard[29] and 28 pm of Djenize et al.[30] Assuming a value of 31 pm for this linewidth at $N_e = 10^{17}$ cm^{-3} results in superior agreement between model and observation for the peak widths of the three main features in our spectrum for any single value of N_e, and this choice is also in better agreement with Refs. 29 and 30. In addition, there were no Stark shift data available for the $^5P^\circ$–$^5D^\circ$ lines that make up the broad peak near 518 nm. Our data suggest a very slight blue shift, and thus, we use a shift of -1 pm at $N_e = 10^{17}$ cm^{-3}. Whereas both adjustments yield visibly better spectral fits, these choices affect the final fit temperature and electron number density by very small amounts, typically less than 1–2%.

As mentioned in the assumptions given to deduce the electron temperature and number density, we have assumed local thermodynamic equilibrium throughout. Previous analyses using the criteria in Ref. 31 suggest that LTE is quickly achieved in a laser spark and that it breaks down at times of the order of tens of microseconds when the electron number density drops below its critical value. For the energy levels that we probe in this work, we would expect LTE to similarly apply to our early-time measurements. The high quality of the spectral fits, which implicitly assume a Boltzmann distribution, also suggest that the LTE assumption is valid over this period. Of greater concern is the assumption of uniform plasma conditions across the diameter of the spark. Yalcin et al.[22] used an Abel inversion technique to compensate for non-uniform conditions and found that the centerline temperatures were approximately 5% higher than the path-integrated values and that the centerline number densities were approximately 20% higher. Though both of these values are still within the uncertainty of our measurements, it does suggest that the centerline temperatures and number densities in the laser spark may be systematically slightly higher than the values we report.

The spectral model also explicitly includes optical depth effects. These are significant in the early stages of the laser spark, at least with respect to the N II emission lines probed in this study. Hermann et al.[26] have shown that such effects can be very important at early times when temperatures and ion densities are very high, but for later times ($t > 350$ ns after the laser pulse) Yalcin et al.[22] suggested that optical depth effects for N I and N II lines were negligible. In our analysis, we found optical depth effects to be significant out to at least 200 ns for the spectral region we investigated. Figure 3 shows the comparison of the spectral-fitting process for cases where optical depth was included and the case in which it was neglected. At 110 ns after the laser pulse, the optically thin fit yields a temperature of 42,700 K. When optical depth is included in the fit, the temperature drops to 38,300 K. Temperatures derived using the optically thin assumption can be at least 20,000 K too high in the vicinity of the peak temperature. However, beyond 200 ns, the optical depth has reduced to the extent that the temperatures derived from the optically thin assumption are identical to those in which optical depth is explicitly considered. Following the approach of Aragon,[32] we include an optical depth $\tau(\nu)$ in our intensity formula. Because $\tau(\nu)$ is proportional to the number density of the emitting ion (here, N II), and because that number density, as well as the exact absorption path length, are unknown, we include as a variable in our fit the term $(N_{\mathrm{NII}}/N_e)L$, where L is the path length.

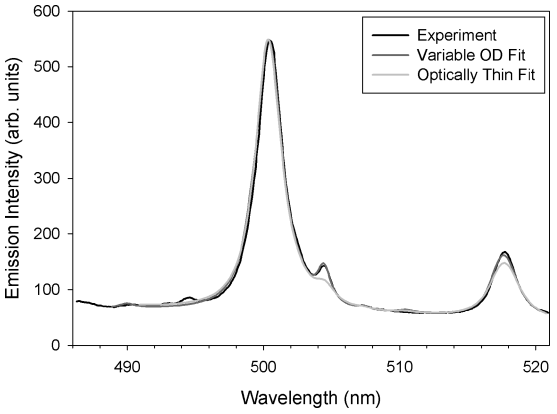

Fig. 3 Best-fit spectra for experimental profile at 110 ns after laser pulse.

The experimental spectra are then fit to six parameters: A temperature, an electron number density, a value of $(N_{\mathrm{NII}}/N_e)L$,two parameters that describe the continuous background below the line spectra, and a global scaling parameter. To fit these spectra, we supply an initial guess of the six parameters and then use a nonlinear optimization routine to minimize the residual between experiment and model. The routine converges very rapidly, and the fits from the spectral model are typically excellent. The agreement of our temperatures and electron number densities with those of previous investigators[21,22] for the later times, when the plasma is optically thin, is generally good. For the earlier times, when optical density is clearly important, we are not aware of any other data in the literature against which to compare our results.

Uncertainties in the temperature can be estimated by standard regression analysis, and because the fits in this spectral region are quite sensitive to choice of temperature and are typically excellent, these uncertainties are small. However, the actual uncertainty in the fit, including the effects of deviation from our set of core assumptions listed earlier, is likely to be higher, although much more difficult to estimate. To the extent to which the plasma can be characterized by a single temperature, we conservatively estimate our uncertainty at $\pm 10\%$, in agreement with Yalcin et al.[22] In terms of number density, the primary uncertainty involved is conversion of Stark widths to N_e, and uncertainties in the neighborhood $\pm 50\%$ are common, for example, in Ref. 22, although the error is typically more systematic than random. Because multiple lines are used in the fit here, we would expect that the systematic error is somewhat reduced, and so we expect our N_e values to be accurate to better than 50%.

Filtered Rayleigh Scattering Measurements

To obtain information of the characteristics of the laser-induced optical breakdown for longer timescales (greater than 20 μs) when thermal/fluid dynamic processes are dominant, a molecular filter-based technique termed filtered Rayleigh scattering (FRS) has been employed. FRS was initially utilized by Miles and Lempert[33] to improve flow visualizations, and later developed by Forkey et al.[34] to measure multiple thermodynamic quantities simultaneously. FRS has been also been applied to combustion and plasma environments to measure gas temperatures.[35–38] Rayleigh scattering in unseeded flows is produced by the gas molecules. In the frequency domain, it can be seen as composed by rotational Raman bands and a central line referred to as Cabannes (see Ref. 39). The side bands (Stokes and anti-Stokes pure rotational Raman) are spectrally separated and may be reduced with an interference filter. The central pure rotational band (Q branch) cannot be separated from the Cabannes line but contributes less than 1% of the total scattering[40] and, thus, is

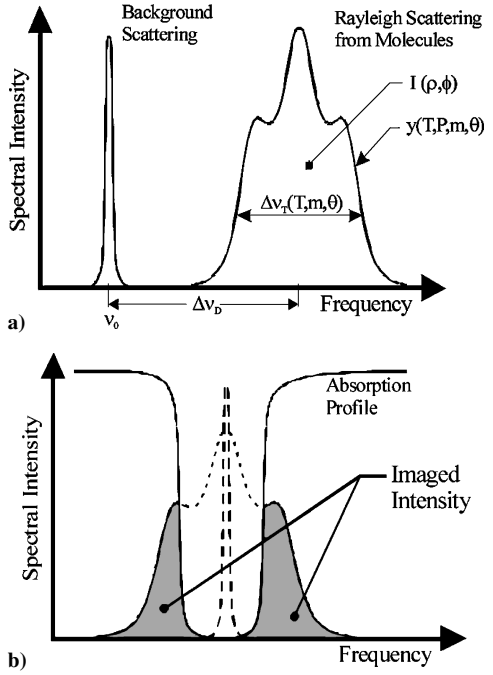

Fig. 4 Schematic of spectral profile of background scattering and molecular Rayleigh scattering: a) function of thermodynamic properties and b) transmission through absorption filter creating the FRS signal imaged by the camera.

normally not modeled. Thus, the spectral line shape of the Rayleigh scattering can be thought of as that of the Cabannes line.

As shown in Fig. 4a, the shape of the Rayleigh–Brillouin (or Cabannes line) is governed by the y parameter, which is given by Tenti et al.[41] as

$$y = \frac{\lambda p}{4\pi\eta \sin(\theta/2)} \left(\frac{m}{2kT}\right)^{\frac{1}{2}} \tag{1}$$

where p is the pressure in the medium, η is the shear viscosity, θ is the angle between the incident light direction and observation direction, and $(2kT/m)^{1/2}$ is the most probable molecular velocity, where k is the Boltzmann constant, T is the temperature, and m is the molecular mass. For the range of y parameters found in the present experiment, the S6 model developed by Tenti et al. has been found to describe the Rayleigh scattering spectrum adequately for diatomic molecules such as nitrogen (although it does not include rotational Raman components). Additionally, the width of the Cabannes line is governed by thermal broadening with the FWHM given by

$$\Delta\nu_T = [2\sin(\theta/2)/\lambda]\sqrt{8kT\,\ell_n 2/m} \tag{2}$$

Also the line central frequency can be Doppler shifted relative to that of the incident laser due to the flow velocity, and the shift is given by

$$\Delta\nu_D = (1/\lambda)\boldsymbol{V}\cdot(\hat{\boldsymbol{k}}_o - \hat{\boldsymbol{k}}_s) \tag{3}$$

where $\boldsymbol{V}$ is the flow velocity, and $\hat{\boldsymbol{k}}_s$ is the incident light unit vector, and $\hat{\boldsymbol{k}}_o$ is the observation unit vector. Additionally the intensity of the light collected is directly proportional to the Rayleigh scattering cross section of the fluid species and the number density of the gas, as shown in Fig. 4a. Also shown in Fig. 4a is the diffuse background scattering from solid surfaces, which is not Doppler shifted or thermally broadened, and therefore, its spectrum is approximately equal to that of the laser.

In FRS an injection-seeded frequency-doubled Nd:YAG pulse laser ($\lambda = 532$ nm) illuminates the flowfield to be investigated. The beam is formed into a planar sheet, and the Rayleigh scattered light is collected by an intensified CCD camera, which views the scattered light at 90 deg from the interrogation plane through an iodine vapor filter. The filter is simply a sealed glass cylinder with optical windows on each end, which contains a preset amount of iodine in gaseous form in it.[34,42] The sidewalls of the cell body are kept at a temperature well above that of iodine crystallization so that its number density remains constant through the experiment.

Iodine has a number of absorption lines in the visible range due to ro-vibronic transitions caused by the bound–bound $B(^3\Pi^+_{0u}) \leftarrow X(^1\Sigma^+_{0g})$ and the bound–unbound $^1\Pi_{1u} \leftarrow X(^1\Sigma^+_{0g})$ transitions.[43] Several of these lines have a good level of extinction (10^{-2} or better), sharp cutoff edges, and a FWHM of only 1–2 GHz, making them excellent choices to use as a spectral notch filter. The injection seeded Nd:YAG laser has a narrow linewidth (~100 MHz) and can be tuned in frequency to an absorption feature of iodine. When the laser is tuned to the center of the iodine filter (as in Fig. 4b) most of this narrow linewidth background scattering is absorbed while a significant portion of the thermally broadened molecular scattering passes through and is recorded by the camera. The filter makes measurements possible even when background scattering is present particularly near surfaces. This demonstrates a significant advantage of FRS over unfiltered Rayleigh scattering techniques.

To obtain a quantitative measurement of temperature using FRS, three assumptions must be made to reduce the number of unknowns so that the temperature can be solved from the collected signal:

1) The scattered light is from a species whose concentration is approximately constant. This allows for the assumption that the Rayleigh scattering cross section is constant.

2) The pressure is relatively constant, which for an ideal gas allows the temperature and density to be directly related.

3) The Doppler frequency shift $\Delta\nu_D$ due to the flow velocity has a negligible effect on the FRS signal. As observed in Eq. (3), this can be accomplished by aligning the laser and camera directions so that they do not have a sensitivity to major, for example, streamwise, velocity components and aligning the laser frequency near the center of the absorption profile so that as part of the signal is shifted out of the filter another portion of the profile is shifted in.

With these assumptions, and the ideal gas law, the FRS signal can be directly related to the temperature (or density). To make these assumptions in the present study (particularly the constant pressure assumption) previous computational and experimental studies have shown that the technique can be applied after approximately 20 μs from the initiation of the laser-induced breakdown.[44]

Within the time frame of 20–100 μs in the hottest regions of the plasma, the effects of concentration may contribute additional uncertainty to the measurement. Below 3500 K, an equilibrium analysis predicts that the Rayleigh cross section varies only slightly from room temperature air. However, the gas may not be in complete equilibrium in the 20–100 μs time frame. Kinetic simulations suggest that at 1 atm below 3500 K, the time constant for N recombination is of the order of 10 μs so that any remaining N at the time of our first collected data point (20 μs) is rapidly recombining. Still, because of the uncertainty in the early-time composition and the pressure/time history, the exact composition in the high-temperature regions of the plasma for the first few data points (out to 100 μs) is not completely known, and this will add additional uncertainty to the peak plasma temperatures in this range.

Additionally, as pointed out in other studies of laser sparks using Rayleigh scattering, Thomson scattering (scattering from electrons) should be considered particularly at high temperatures because it has a scattering cross section approximately 100 larger than that of Rayleigh scattering for a laser irradiation wavelength of 532 nm. Previous studies that have utilized Rayleigh scattering for temperature measurements of laser sparks in various gases such as nitrogen, argon, and helium have reported that the effect of Thomson scattering on the Rayleigh scattering signal is not significant for temperatures from below 5000 K (argon) to 7000 K (nitrogen). Additionally for the present study, it can be shown using the Saha equation (see Ref. 45) that for temperatures on the order of 4500 K the degree of ionization is about 10^{-7}; thus, the portion of the signal due to Thomson scattering can be safely neglected.

Figure 5 shows the FRS signal (normalized by the FRS signal at ambient conditions) as a function of temperature with the laser tuned to the absorption feature of iodine located at 18,789.28 cm^{-1}, which was used in these experiments. Further details of using FRS (such as correcting for background scattering) to measure temperature in the laser-induced breakdown environment investigated here, as well as other flows, have been described in detail elsewhere.[46] For the temperature results shown here, the measurement uncertainty has been calculated to be better than ±8% over the temperature range measured (except for the earliest times and highest temperatures for reasons already discussed). Note that the relative uncertainty becomes slightly lower as the temperature decreases.

Figure 6 shows a schematic of the experimental configuration utilized for the FRS measurements with the laser-induced optical breakdown region, laser illumination plane, and camera position shown. Two pulsed Nd:YAG lasers were utilized for these experiments, one to interrogate the region of interest using the FRS technique and one to initiate the laser spark. The interrogation laser was an injection-seeded frequency doubled (532 nm) with a maximum laser energy of approximately 550 mJ/pulse. The beam was directed to the measurement region with dichroic mirrors and transformed into a thin sheet with a diverging–converging spherical and cylindrical lens pair that allowed for planar measurements. The Rayleigh scattering was collected through an iodine filter (termed the camera filter), which was 20 cm in length. The Rayleigh scattered light was imaged with a Princeton Instruments intensified CCD camera located perpendicularly to the interrogation plane (Fig. 6). The laser and the camera gate (set to have an exposure time of 80 ns) were synchronized via a 10-Hz pulse and delay generator (not shown in Fig. 6).

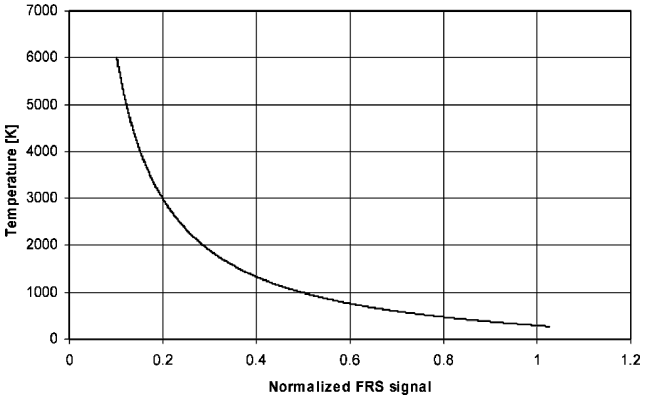

Fig. 5 Normalized FRS signal as function of gas temperature for laser tuned near center of absorption feature of iodine filter located at 18,789.28 cm^{-1}.

The laser utilized to create the laser spark was a double-cavity, double-pulse Spectra Physics Model Quanta Ray PIV-200 with a repetition rate of 10 Hz and similar beam and laser pulse characteristics as described earlier with a beam diameter of about 9 mm and pulse duration measured to be approximately 7.2-ns FWHM. As before, the laser utilized for creating the spark was frequency doubled to a wavelength of 532 nm and operated at 180 mJ per pulse resulting in a net energy of 150 mJ per pulse for each case. A slow coflow of filtered dry air was bled through the interrogation region to keep dust particles from overwelming the Rayleigh scattering signal possibly damaging the intensified camera, which also helped to keep dust particles from interfering with the spark generation. This coflow had a negligible velocity and was uniformly distributed over a large region with negligible effects observed to the laser spark fluid flow. The temperature and pressure were at standared atmospheric conditions (approximately 21°C and 1 atm). Because the pulse repetition rate is relatively slow (10 Hz) there was sufficient time between pulses to have the same initial conditions with no air depletion or temperature buildup effects observed over time. The few remaining particles that were imaged were removed by threshold filtering in the averaging routine but were very sparse and so did not contaminate the measurements.

The laser frequency was controlled and monitored with a system consisting of a reference filter cell (RC) and two photodiodes (PD1) and (PD2), as shown in the dotted region of Fig. 6. The reflection from an optical wedge was directed to the frequency monitoring system, where the beam was expanded in diameter to about 5 cm and passed through the RC. PD1 was used to compensate for laser intensity fluctuations, and the ratio PD2/PD1 was used as a transmission through the cell. The RC absorption line was made optically thin by reducing the partial pressure of iodine to about 0.696 torr. (Calibration was done with a water bath at 308 K with I_2 crystals in a side arm attached to the cell body.) This allowed good frequency discrimination to within 4 MHz (Ref. 47) near the center of

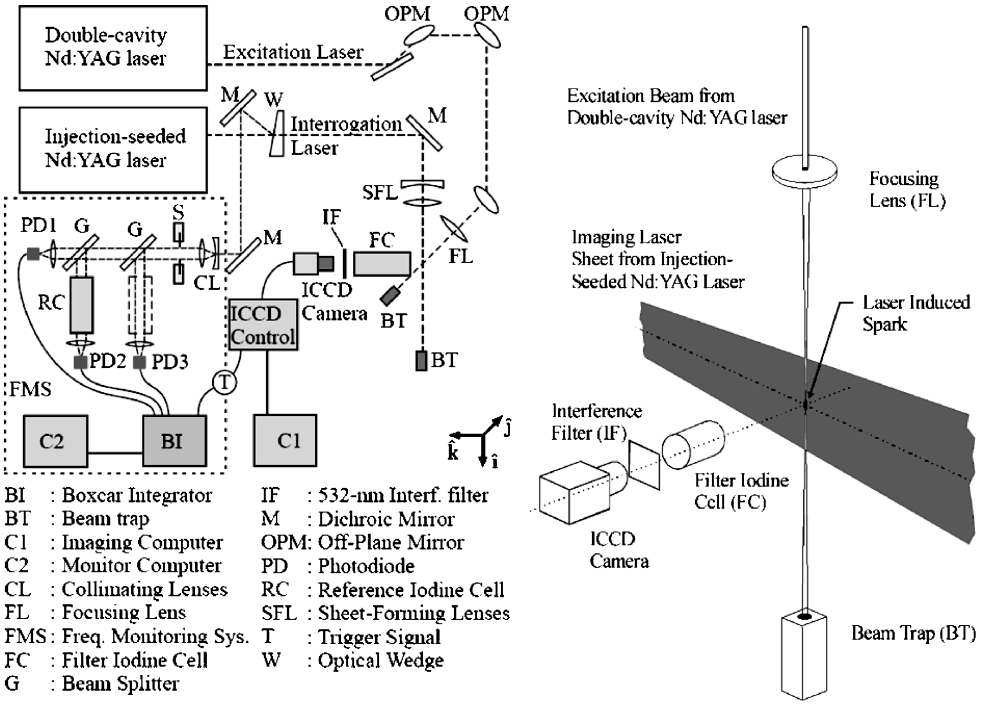

Fig. 6 Experimental layout for filtered Rayleigh scattering utilized for flow visualizations and temperature field measurements at later times.

the absorption line. The conversion from transmission to frequency was done by performing a full scan of the filter over the Nd:YAG tuning range and using the model by Forkey et al.[48] to convert bias voltages to frequency. A third photodiode (PD3) was used to simultaneously calibrate the filter cell (FC) and RC before the experiment and, thus, obtain the filter absorption profile.

Results and Discussion

Early-Time Measurements: Emission

Figure 7 shows the temporal decay of the relative emission intensity as recorded by a fast photodiode. The intensity peaks during the laser pulse and falls rapidly thereafter. The temporal intensity profile does not fit well to a single or double exponential. In general, the decay is much faster at earlier times than later times. Roughly 80% of the total emission occurs during the first 500 ns after the laser pulse. Whereas many laser spark diagnostics, for example, LIBS, employ delays to avoid the continuum emission early in the event and to thereby highlight emission features that appear later, note that such techniques probe only a very small fraction of the total light emitted from the spark.

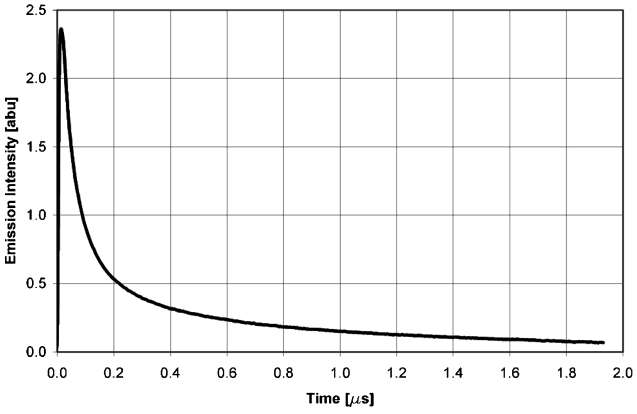

Fig. 7 Temporal evolution of total intensity from emission of laser spark in air.

Images were taken of the laser-induced optical breakdown process using an intensified CCD camera (ICCD) with a 50-mm-focal-length lens with extension rings to allow an appropriate field of view. Neutral density filters were utilized to decrease the intensity, and 200 instantaneous images were accumulated together at each delay time from the laser pulse initiating the optical breakdown. The emission images are given in Fig. 8 for a range of delay times ranging from 25 to 1000 ns. Each image has been normalized by its maximum value to preserve the detail as the emission decays following a law quantified in Fig. 7. Similar to what has been reported by other investigators, the emission starts with a teardrop shape (at 25 ns) and quickly evolves into two distinct regions with the laser spark growing more intensely toward the laser propagation direction. The evolution of the length, maximum width, and total cross-sectional area of the emission is given in Fig. 9. The measurements were based on the edges of the laser spark as defined by the contours of 10% of the maximum intensity at each time delay. Figure 9 indicates that the size of the laser spark experiences rapid growth for the first 400 ns, after which it has a more gradual linear growth rate. The laser spark achieves a length, maximum width, and cross-sectional area of 5.2 mm, 2.5 mm, and 11 mm^2,

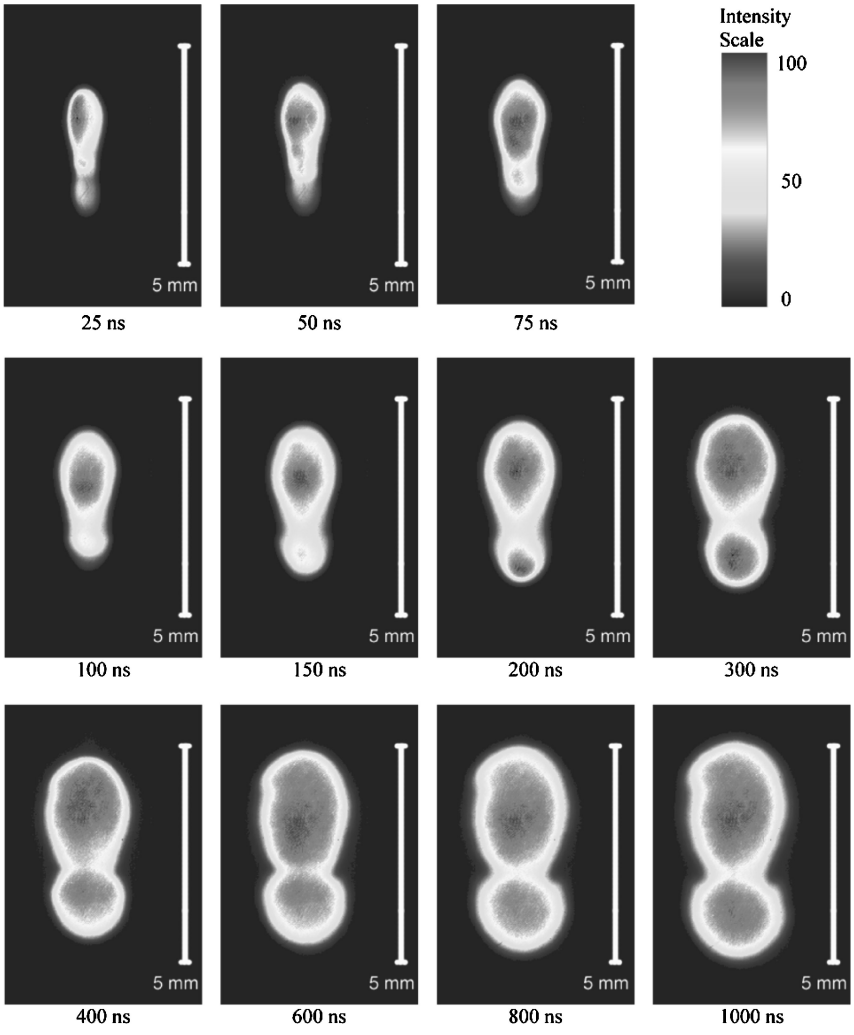

Fig. 8 Emission from laser spark over range of delay times from initiating laser pulse; beam propagation direction is from top to bottom and images normalized by maximum intensity value at each delay time.

respectively, by 1 μs. The uncertainty in the length measurements is approximately ± 0.05 mm.

The temporal temperature data for a single spark condition are shown in Fig. 10. The first point for which a spectral curve fit is made is 50 ns after the laser pulse. At this time, two peaks are clearly resolved from the continuous background, and a meaningful fit can be obtained. For earlier times, these peaks cannot be accurately extracted from the continuum. A set of representative spectra and their fits is shown in Fig. 11.

The temperature decay follows roughly a double exponential behavior as suggested by the LIBS experiments of Hermann et al.[26] The highest temperature measured (at 50 ns from the laser pulse) is roughly 45,000 K. In the period of 50–300 ns, the temperature drops by roughly a factor of two, fitting to an exponential decay with a time constant of ~87 ns. Afterward, there is a transition to a much slower temporal decay, with a time constant of ~410 ns for times out to the microsecond range. Extrapolating this curve from 50 ns back to the peak of the emission pulse (~10 ns after the start of the laser pulse) yields temperatures only slightly above 50,000 K.

Electron number density vs time is shown in Fig. 12. The N_e curve extrapolates to electron number densities of roughly 10^{19} cm^{-3} near the laser pulse. In the period of 50–300 ns, there is a reduction in electron number density of a factor of about 10. The decay of number density with time follows a $t^{-0.84}$ dependence over the first 1 μs, which is fairly close to the t^{-1} dependence from simple ion–electron recombination with a constant recombination rate. Because the recombination rate decreases with decreasing pressure, it is not unexpected that the recombination should be slightly weaker than t^{-1}. At the measured rate, the N_e decays to 10^{18} cm^{-3} by 400 ns and 10^{17} cm^{-3} by 1.5 μs.

It would be useful to compare the measured electron number densities with those of a detailed equilibrium analysis to assess the degree to which the plasma has attained an equilibrium composition. Such an analysis was presented by Yalcin et al.[22] with the assumption of a pressure of 1 atm. In that case, the early-time electron number density (at 350 ns after the laser pulse) was approximately an order of magnitude greater than the 1 atm equilibrium calculation, but the 1.4-μs data was less than a factor of two high. However, computations such as those of Phuoc[49] suggest that there is significant overpressure throughout the spark for at least several hundred nanoseconds after the laser pulse. Such overpressure may persist into the microsecond timescale, although the pressure should approach 1 atm fairly rapidly after 1 μs or so. Because our number density at 1.5 μs (4×10^{17} cm^{-3}) agrees with the Yalcin et al. measurements at 1.4 μs (3×10^{17} cm^{-3}) to within experimental uncertainty, our speculation is similar to that of Yalcin et al. that equilibrium is approached in the 1–2-μs region, provided that the pressure is indeed approaching 1 atm. Further measurements of pressure would be warranted to test this speculation.

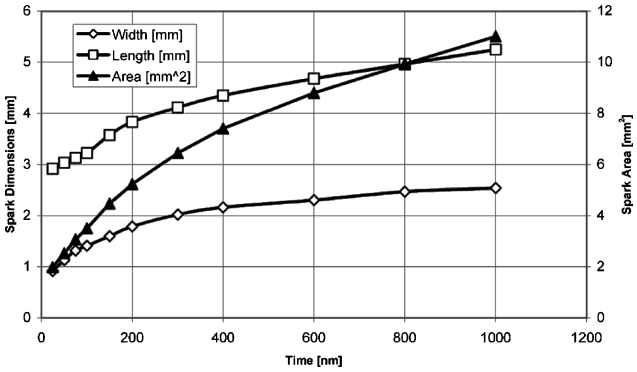

Fig. 9 Spatial characteristics (length, maximum width, and cross-sectional area) of evolution of laser spark emission defined by 10% of maximum intensity at each time delay.

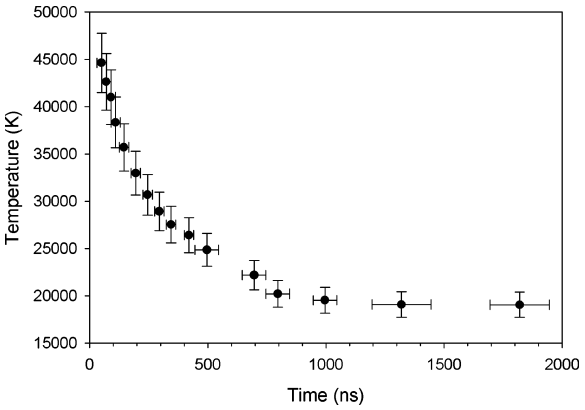

Fig. 10 Temporal decay of emission temperature of laser spark in air from 50 to 1750 ns after laser pulse.

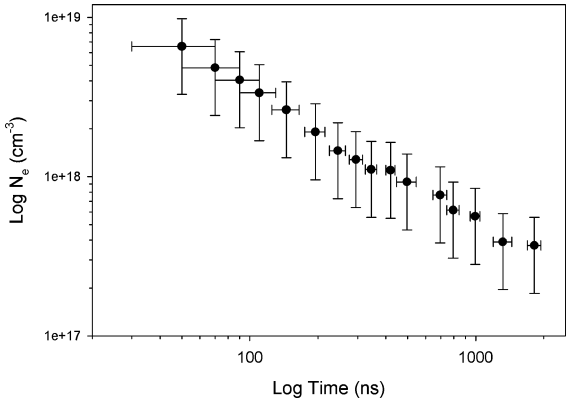

Fig. 12 Temporal decay of electron number density in laser spark from 50 to 1750 ns after laser pulse.

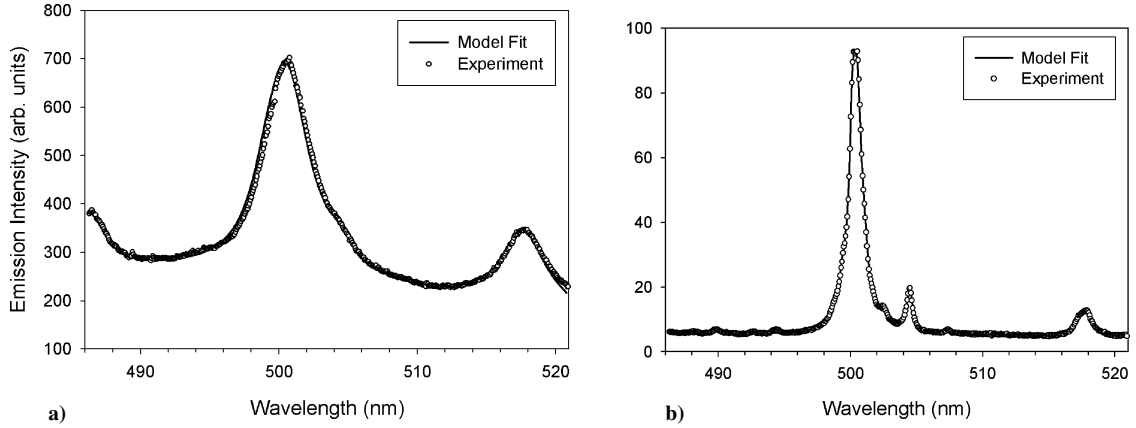

Fig. 11 Sample fits of spectral model to emission data. a) delay = 50 ns, $T = 44{,}600$ K, and $N_e = 6.6 \times 10^{18}$ cm^{-3} and b) delay = 295 ns, $T = 28{,}900$, and $N_e = 1.3 \times 10^{18}$ cm^{-3}.

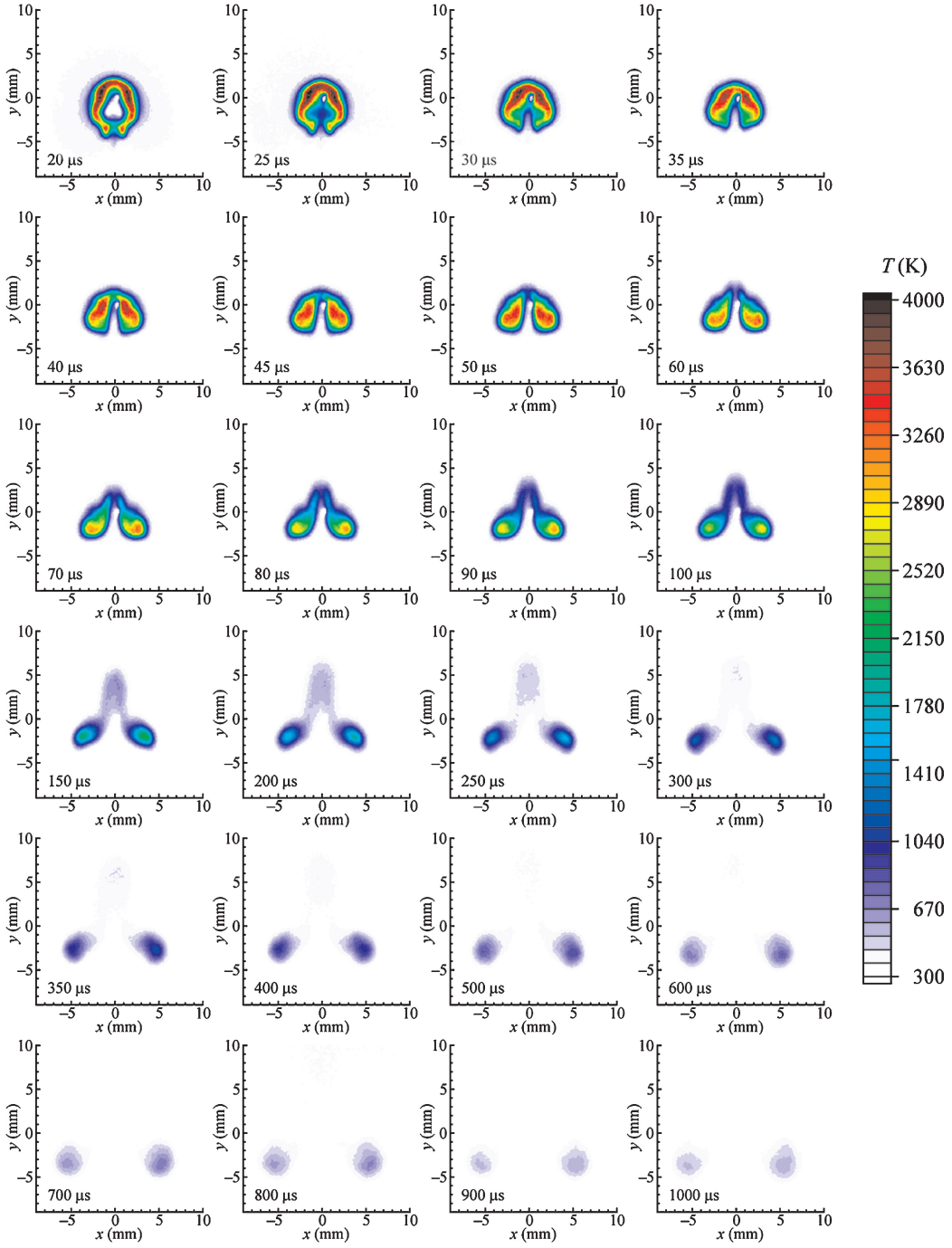

Fig. 13 Temperature field of laser-induced optical breakdown measured by using FRS.

Longer-Timescale Measurements: FRS

To quantify the evolution of the temperature field, the FRS temperature technique was used for times greater than 20 μs (due to the earlier mentioned assumptions). Figure 13 shows the FRS measured temperature field for time delays taken from 20 to 1000 μs from the initial laser pulse. Note that by this time the blast wave has propagated out of the field of view. At each time delay, 200 frames were acquired and ensemble averaged together.

At the initial time delay of 20 μs, the hot region shows a maximum temperature of approximately 4100 K. The small white region at the center of the first image of Fig. 13 is due to bright emission from the plasma, which still persists on the ICCD camera and eclipses the Rayleigh scattering. As time progresses, the asymmetric formation of the plasma induces the ejection of fluid in the opposite direction to the laser propagation direction, as has been reported in previous investigations.[50,51] This is believed to be due to the plasma formation and growth in the direction of the excitation beam and not significantly due to the cross-beam initial energy distribution. This motion induces the formation of the toroidal structure (or vortex ring) and jet through the center of the structure. As the jet propagates through the center of the ring vortex (from 35 to 100 μs) a portion of the hotter vortex fluid is shed propagating ahead of the jet. Simultaneously the vortex ring (as marked by the position of the two high-temperature round regions in the vortex core) propagates in the opposite direction, as shown in Fig. 13.

The vertical position of the ring vortex structure is plotted in Fig. 14 and indicates that from 50 to 1000 μs the vortex ring manages to propagate gradually in the direction of the excitation laser beam. Also given in Fig. 14 are the results from Longenecker et al.[25] for a laser spark created at 1064 nm, 250 mJ, with a pulse duration of 20 ns created in nitrogen, argon, and a 50:50 nitrogen argon mixture. (Note that these results were inverted and shifted by approximately 3.7 mm

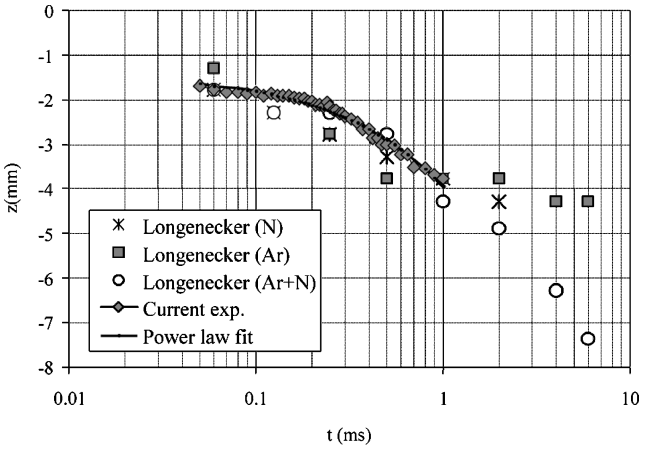

Fig. 14 Position of vortex (torus) from laser-induced spark created in air with its correspondent power law curve fit compared with vortex position reported by Longenecker et al.,[25] for argon, nitrogen, and a 50:50 mixture of argon and nitrogen.

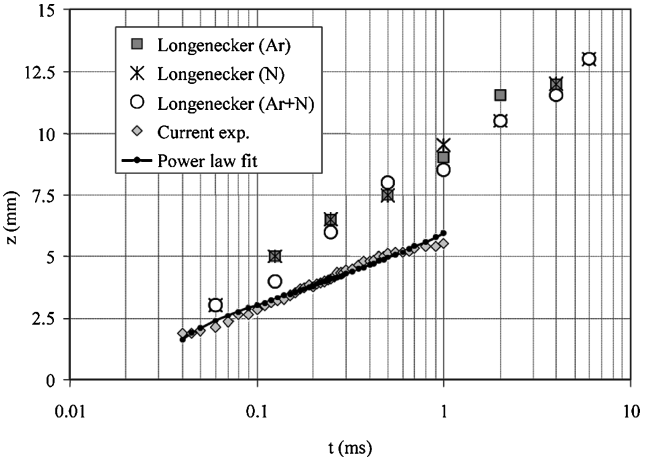

Fig. 15 Radius of vortex (torus) from laser-induced spark created in air with its correspondent power law curve fit compared with vortex radius reported by Longenecker et al.,[25] for argon, nitrogen, and a 50:50 mixture of argon and nitrogen and Longenecker et al. data fit.

to coincide with the coordinate system of the current experiment.) The evolution of the radial spread, that is, radius of the vortex ring, is shown in Fig. 15, again compared to the other gases reported by Longenecker et al. The growth of the vortex ring radius progresses until approximately 250 μs, where it slowly tapers off and the radius remains relatively constant. As the flow patterns evolve in time, heat transfer with the surroundings due to entrainment of ambient fluid and thermal conduction reduces the temperature until it finally diffuses into cooler ambient air. Longenecker et al. utilized a simple power law to fit both the torus position and radial spread that was of the form of

$$x(t) = x_0(t - t_0)^p \tag{4}$$

where x_0, t_0, and p are fitting parameters. They noted that although there is no basis in utilizing this equation from the physics of the problem it does tend to describe the trends observed over two orders of magnitude for their case. The curves of the power law fit to the current data are given on Figs. 14 and 15 for the vortex ring position and radial spread with coefficients given in Table 1. As observed, the power law fits the data well for both vortex position and radius. When the present results in air are compared with those in other gases, the vortex position in air tends to have a similar direction and trend compared to the nitrogen and 50:50 nitrogen argon mixture, but shows a deviation at later times from the pure argon results reported by Longenecker et al. In Fig. 15, the vortex radius reported

Table 1 Coefficients for power law curve fit[a] for torus position and radius

Dimension	x_0, mm	t_0, s	p
Position, mm	−226.3	−0.000240	0.605
Radius, mm	34.05	3.42×10^{-5}	0.252

[a]Equation (4).

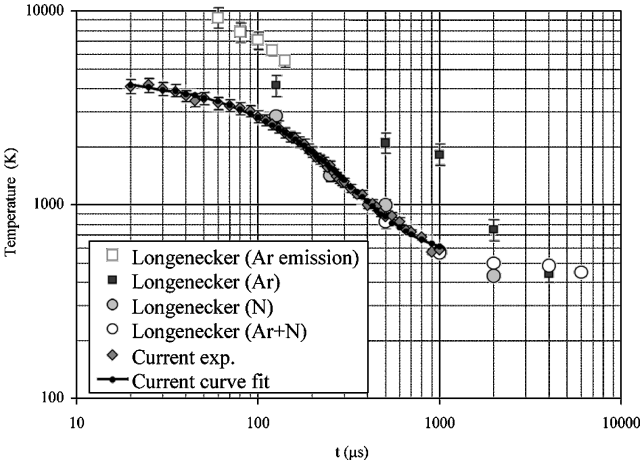

Fig. 16 Temporal evolution of maximum temperature in laser-induced spark in air measured using FRS and correspondent power law curve fit compared with Longenecker et al.[25] temperature values by emission spectroscopy in argon, Rayleigh scattering in argon, in nitrogen, and in a 50:50 mixture of argon and nitrogen.

by Longenecker et al. shows a slightly faster growth rate than that observed in the experiments in air presented here. This difference could be due to the different gases or properties of the initiating laser such as wavelength, beam diameter, spatial intensity distribution, or pulse duration. For instance, differences in the toroidal structure's diameter has been reported by Nassif and Huwel,[24] who showed that as the laser energy (which was higher for the experiments conducted by Longenecker et al.) increases, the torus diameter increases, but the vertical position tended to follow the same trend for different input energies.

To quantify the temperature evolution more clearly, the highest 10% of the temperatures were averaged for each time. The decay of this maximum average temperature is shown in Fig. 16. Comparison with temperatures measured using Rayleigh scattering in nitrogen, argon, and a 50:50 mixture of argon and nitrogen by Longenecker et al.[25] are also shown. The maximum temperature between the present results in air agree quite well with the Longenecker et al. results in nitrogen for the times measured, but is slightly lower than the other gas mixtures at each time delay. One additional point of comparison of the present results can be found at 32 μs, where the present measurements indicate a maximum temperature of 3900 K compared to approximately 3600 K as reported in the computational results of Dors and Parigger.[51]

As already mentioned, Hermann et al.[26] suggested the use of a double exponential to fit the temperature decay for the first microsecond, whereas Longnecker et al. suggested the use of a double-exponential decay for there data obtained after the initial microsecond. As suggested by Longenecker et al., although multiple exponential decays are empirical in nature, that is, not based on any physical models, one would expect that different plasma-cooling phases to occur over particular times. Based on these results for the time period that has been measured in the present experiments, a triple exponential decay was fit to the present data having the form

$$T = T_0 + x_1 \exp(-t/t_1) + x_2 \exp(-t/t_2) + x_3 \exp(-t/t_3) \tag{5}$$

were T_0, x_1, x_2, x_3, t_1, t_2, and t_3 are fitting parameters. Table 2 gives the triple-exponential decay fitting parameters based on the temperature measurements made at both early times (from emission spectra

Table 2 Coefficients for triple exponential curve fit[a] for maximum temperature from laser-induced optical breakdown in air

Coefficient	Value
T_0	300 K
x_1	37,017 K
x_2	3,578 K
x_3	805.9 K
t_1	0.917 μs
t_2	144.39 μs
t_3	949.18 μs

[a]Equation (5).

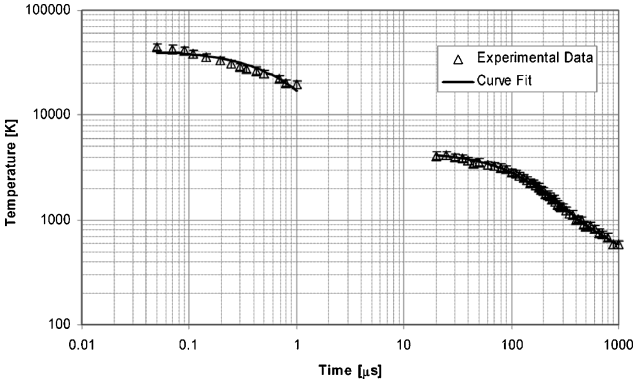

Fig. 17 Full temporal temperature range with curve fit; experimental temperature measured by emission before 1 μs and by using FRS after 20 μs.

measurement) and later times (from FRS measurements) with the data and fit shown in Fig. 17. As observed, the triple exponential appears to fit the data well, but it should be kept in mind that this is an empirical relationship with no basis on a physical model and there are no data between 1 and 10 μs verifying what the shape of the decay might be.

Conclusions

Measurements were taken to characterize the spark created from the second harmonic of a 180-mJ focused Nd:YAG pulsed laser beam. Images taken of the emission created indicate that the spark reaches a length of 5.2 mm with 80% of the emission occurring within the first 400 ns. Emission spectra measurements of the N II lines occurring between 490 and 520 nm indicate a peak temperature of 50,000 K, which decays over the first 1 μs. The electron number density peaks at approximately 10^{19} cm^{-3}, decaying only slightly slower than t^{-1} as suggested by simple ion–electron recombination. Optical depth corrections were found to be significant in the first 200 ns to fit accurately the theoretical and measured spectra used to deduce the temperature and electron number density. With use of FRS, the temperature field was measured from 20 to 1000 μs, where the peak temperature starts at approximately 4100 K at 20 μs and decays to 580 K by 1 ms. The planar temperature images show a center jet propagating in the opposite direction as the initiating laser beam while the induced vortex ring (or torus) propagates in the direction of the beam. The evolution of the position and radius of the torus structure is described and fit with a power law utilized by previous investigators. The temperature of the plasma created by laser-induced optical breakdown appears to fit well a triple exponential over the four orders of magnitude of temporal range where measurements were conducted.

Acknowledgments

The authors thank the Air Force Office of Scientific Research with John Schmisseur for funding this work on energy deposition utilizing laser induced optical breakdown (F49620-01-1-0368 and FA9550-04-0177). G. Elliott and M. Boguszko also acknowledge the support of the National Science Foundation (CTS 97-33388) with Contract Monitor Michael Plezniac for support in their development efforts of molecular-filtered-based techniques utilized in this study. Also, we thank G. Tenti for providing the model of Rayleigh–Brillouin scattering. Additionally, we thank our colleagues Doyle Knight, Graham Candler, Hong Yan, and Ramnath Kandala for their discussions and input regarding this work.

References

[1]Klimov, A. I., Koblov, A. N., Mishin, G. I., Serov, Y. L., and Yavor, I. P., "Shock Wave Propagation in a Glow Discharge," *Soviet Technical Physics Letters*, Vol. 8, No. 4, 1982, pp. 192–194.

[2]Gordeev, V. P., Krasilnikov, A. V., Lagutin, V. I., and Otmennikov, V. N., "Experimental Study of the Possibility of Reducing Supersonic Drag by Employing Plasma Technology," *Izvestiya RAS, Mekhanica Zhidkosti i Gaza (Fluid Dynamics)*, Vol. 31, No. 2, 1996, pp. 177–182.

[3]Poggie, J., "Energy Addition for Shockwave Control," AIAA Paper 99-3612, 1999.

[4]Adelgren, R. G., Elliott, G. S., Crawford, J. B., Carter, C. D., Grosjean, D., and Donbar, J. M., "Axisymmetric Jet Shear Layer Excitation Induced by Electric Arc Discharge and Focused Laser Energy Deposition," AIAA Paper 2002-0729, Jan. 2002.

[5]Aradag, S., Yan, H., and Knight, D., "Energy Deposition in Supersonic Cavity Flow," AIAA Paper 2004-0514, Jan. 2004.

[6]Macheret, S. O., Shneider, M. N., and Miles, R. B., "Scramjet Inlet Control by Off-Body Energy Addition: A Virtual Cowl," AIAA Paper 2003-0032, Jan. 2003.

[7]Marconi, F., "An Investigation of Tailored Upstream Heating for Sonic Boom and Drag Reduction," AIAA Paper 98-0333, 1998.

[8]Zaidi, S. H., Shneider, M. N., Mansfield, D. K., Ionikh, Y. Z., and Miles, R. B., "Influence of Upstream Pulsed Energy Deposition on a Shockwave Structure in Supersonic Flow," AIAA Paper 2002-2703, June 2002.

[9]Adelgren, R., Elliott, G., Knight, D., Zheltovodov, A., and Beutner T. J., "Energy Deposition in Supersonic Flows," AIAA Paper 2001-0885, Jan. 2001.

[10]Adelgren, R., Yan, H., Elliott, G., Knight, D., Buetner, T., Zheltovodov, A., Ivanov, M., and Khotyanovsky, D., "Localized Flow Control by Laser Energy Deposition Applied to Edney IV Shock Impingement and Intersecting Shocks," AIAA Paper 2003-0031, Jan. 2003.

[11]Yan, H., Adelgren, R., Elliott, G. S., Knight, D., and Beutner, T., "Effect of Energy Addition on MR to RR Transition," *Shock Waves*, Vol. 13, No. 2, 2003, pp. 113–121.

[12]Kolesnichenko, Y., Brovkin, V., Azarova, O., Grudnitsky, V., Lashkov, V., and Mashek, I., "MW Energy Deposition for Aerodynamic Application," AIAA Paper 2003-0362, Jan. 2003.

[13]Knight, D., Kuchinskiy, V., Kuranov, A., and Sheikin, E., "Survey of Aerodynamic Flow Control at High Speed by Energy Deposition," AIAA Paper 2003-0525, Jan. 2003.

[14]Knight, D., "A Selected Survey of Magnetogasdynamic Local Flow Control at High Speeds," AIAA Paper 2004-1191, Jan. 2004.

[15]Raizer, Y. P., "Breakdown and Heating of Gases Under the Influence of a Laser Beam," *Soviet Physics Uspekhi*, Vol. 8, No. 5, 1966, pp. 650–673.

[16]Raizer, Y. P., *Laser-Induced Discharge Phenomena*, Consultants Bureau, New York, 1977.

[17]Morgan, G. C., "Laser-Induced Breakdown of Gases," *Reports on Progress in Physics*, Vol. 38, 1975, pp. 621–665.

[18]Smith, D. C., "Laser Induced Gas Breakdown and Plasma Interaction," AIAA Paper 2000-0716, Jan. 2000.

[19]Dors, I., Parigger, C., and Lewis, J., "Fluid Dynamics Effects Following Laser-induced Optical Breakdown," AIAA Paper 2000-0717, Jan. 2000.

[20]Lee, W. B., Wu, J. Y., Lee, Y. I., and Sneddon, J., "Recent Applications of Laser-Induced Breakdown Spectrometry: A Review of Material Approaches," *Applied Spectroscopy Reviews*, Vol. 39, No. 1, 2004, pp. 27–97.

[21]Radziemski, L. J., Loree, T. R., Cremers, D. A., and Hoffman, N. M., "Time-Resolved Laser-Induced Breakdown Spectrometry of Aerosols," *Analytical Chemistry*, Vol. 55, No. 8, 1983, pp. 1246–1252.

[22]Yalcin, S., Crosley, D. R., Smith, G. P., and Faris, G. W., "Influence of Ambient Conditions on the Laser Air Spark," *Applied Physics B*, Vol. 68, No. 1, 1999, pp. 121–130.

[23]Chen, Y.-L., Lewis, J. W. L., and Parigger, C., "Spatial and Temporal Profiles of Pulsed Laser-Induced Air Plasma Emissions," *Journal of Quantitative Spectroscopy and Radiative Transfer*, Vol. 67, No. 2, 2000, pp. 91–103.

[24]Nassif, D., and Huwel, L., "Appearance of Toroidal Structure in Dissipating Laser-Generated Sparks," *Journal of Applied Physics*, Vol. 87, No. 5, 2000, pp. 2127–2130.

[25]Longnecker, M., Huwel, L., Cadwell, L., and Nassif, D., "Laser-Generated Spark Morphology and Temperature Records from Emission and Rayleigh Scattering Studies," *Applied Optics*, Vol. 42, No. 6, 2003, pp. 990–996.

[26]Hermann, J., Boulmer-Leborgne, C., and Hong, D., "Diagnostics of the Early Phase of an Ultraviolet Laser Induced Plasma by Spectral Line Analysis Considering Self Absorption," *Journal of Applied Physics*, Vol. 83, No. 2, 1998, pp. 691–696.

[27]Konjevic, N., Lesage, A., Fuhr, J. R., and Wiese, W. L., "Experimental Stark Widths and Shifts for Spectral Lines of Neutral and Ionized Atoms," *Journal of Chemical and Physical Reference Data*, Vol. 31, No. 3, 2002, pp. 819–927.

[28]Mar, S., Aparico, J. A., de la Rosa, M. I., del Val, J. A., Gigosos, M. A., Gonzalez, V. R., and Perez, C., "Measurement of Stark Broadening and Shift of Visible NII Lines," *Journal of Physics B: Atomic, Molecular, and Optical Physics*, Vol. 33, No. 6, 2000, pp. 1169–1184.

[29]Purcell, S. T., and Barnard, A. J., "Stark Broadening Measurements of Some N(II) and N(III) Lines," *Journal of Quantitative Spectroscopy and Radiative Transfer*, Vol. 32, No. 3, 1984, pp. 205–209.

[30]Djenize, S., Sreckovic, A., and Labat, J., "Stark Shifts of Singly Ionized Nitrogen Spectral Lines," *Astronomy and Astrophyics*, Vol. 253, No. 2, 1992, pp. 632–634.

[31]Griem, H. R., *Principles of Plasma Spectroscopy*, Cambridge Univ. Press, Cambridge, England, U.K., 1997.

[32]Aragon, C., Bengoechea, J., and Aguilera, J. A., "Influence of the Optical Depth on Spectral Line Emission from Laser-Induced Plasmas," *Spectrochimica Acta Part B*, Vol. 56, No. 6, 2001, pp. 619–628.

[33]Miles, R. B., and Lempert, W. R., "Two-Dimensional Measurement of Density, Velocity and Temperature in Turbulent High-Speed Air Flows by UV Rayleigh Scattering," *Applied Physics B*, Vol. 51, July 1990, pp. 1–7.

[34]Forkey, J. N., Finkelstein, N. D., Lempert, W. R., and Miles, R. B., "Demonstration and Characterization of Filtered Rayleigh Scattering for Planar Velocity Measurements," *AIAA Journal*, Vol. 34, No. 3, 1994, pp. 442–448.

[35]Yalin, A. P., Ionikh, Y., Mechchanov, A., and Miles, R., "2-D Temperature Fields in Glow Discharges Measured with Ultra Violet Filtered Rayleigh Scattering," AIAA Paper 2000-0375, Jan. 2000.

[36]Elliott, G. S., Glumac, N., and Carter, C. D., "Molecular Filtered Rayleigh Scattering Applied to Combustion," *Measurement Science and Technology*, Vol. 12, No. 4, 2001, pp. 452–466.

[37]Hoffman, D., Munch, K. U., and Leipertz, A., "Two-Dimensional Temperature Determination in Sooting Flames by Filtered Rayleigh Scattering," *Optics Letters*, Vol. 21, No. 7, 1996, pp. 525–527.

[38]Kearney, S. P., Beresh, S. J., Grasser, T. W., Schefer, R. W., Schrader, P. E., and Farrow, R. L., "A Filtered Rayleigh Scattering Apparatus for Gas-Phase and Combustion Temperature Imaging," AIAA Paper 2003-0584, Jan. 2003.

[39]Young, A. T., "Rayleigh Scattering," *Applied Optics*, Vol. 20, No. 4, 1981, pp. 533–535.

[40]Long, D. A., *Raman Spectroscopy*, McGraw–Hill, New York, 1977.

[41]Tenti, G., Boley, C., and Desai, R., "On the Kinetic Model Description of Rayleigh–Brillouin Scattering from Molecular Gases," *Canadian Journal of Physics*, Vol. 52, No. 4, 1974, pp. 285–290.

[42]Elliott, G. S., and Beutner, T. J., "A Review of Recent Advancements in Molecular Filter Based Planar Doppler Velocimetry Systems," *Progress in Aerospace Sciences*, Vol. 35, 1999, pp. 799–845.

[43]Tellinghuisen, J., "Resolution of the Visible–Infrared Absorption Spectrum of I2 into Three Contribution Transitions," *Journal of Chemical Physics*, Vol. 58, No. 7, 1973, pp. 2821–2835.

[44]Yan, H., Adelgren, R., Boguszko, M., Elliott, G. S., and Knight, D., "Laser Energy Deposition in Quiescent Air," *AIAA Journal*, Vol. 41, No. 10, 2003, pp. 1988–1995.

[45]Vincenti, W. G., and Kruger, C. H., Jr., *Introduction to Physical Gas Dynamics*, Krieger, New York, 1975.

[46]Boguszko, M., and Elliott, G. S., "On the Use of Filtered Rayleigh Scattering for Measurements in Compressible Flows and Thermal Fields," *Experiments in Fluids* (to be published).

[47]Mosedale, A., Elliott, G. S., Carter, C. D., and Beutner, T. J., "Planar Doppler Velocimetry in a Large-Scale Facility," *AIAA Journal*, Vol. 38, No. 6, 2000, pp. 1010–1024.

[48]Forkey, J. N., Lempert, W. R., and Miles, R. B., "Corrected and Calibrated I_2 Absorption Model at Frequency-Doubled Nd:YAG Laser Wavelengths," *Applied Optics*, Vol. 36, No. 27, 1997, p. 6729.

[49]Phuoc, T. X., "An Experimental and Numerical Study of Laser-Induced Spark in Air," *Optics and Lasers Engineering*, Vol. 43, No. 2, 2005, pp. 113–129.

[50]Svetsov, V., Popova, M., Rybakov, V., Artemiev, V., and Medveduk, S., "Jet and Vortex Flow Induced by Anisotropic Blast Wave: Experimental and Computational Study," *Shock Waves*, Vol. 7, No. 6, 1997, pp. 325–334.

[51]Dors, I. G., and Parigger, C. G., "Computational Fluid-Dynamic Model of Laser-Induced Breakdown in Air," *Applied Optics*, Vol. 42, No. 30, 2003, pp. 5978–5985.

M. Auweter-Kurtz
Associate Editor